

Event-based vision for egomotion estimation using precise event timing

Hugh Greatorex^{1,2,*}, Michele Mastella³, Madison Cotteret^{1,2,4},
Ole Richter⁵, Elisabetta Chicca^{1,2}

Abstract—Egomotion estimation is crucial for applications such as autonomous navigation and robotics, where accurate and real-time motion tracking is required. However, traditional methods relying on inertial sensors are highly sensitive to external conditions, and suffer from drifts leading to large inaccuracies over long distances. Vision-based methods, particularly those utilising event-based vision sensors, provide an efficient alternative by capturing data only when changes are perceived in the scene. This approach minimises power consumption while delivering high-speed, low-latency feedback. In this work, we propose a fully event-based pipeline for egomotion estimation that processes the event stream directly within the event-based domain. This method eliminates the need for frame-based intermediaries, allowing for low-latency and energy-efficient motion estimation. We construct a shallow spiking neural network using a synaptic gating mechanism to convert precise event timing into bursts of spikes. These spikes encode local optical flow velocities, and the network provides an event-based readout of egomotion. We evaluate the network’s performance on a dedicated chip, demonstrating strong potential for low-latency, low-power motion estimation. Additionally, simulations of larger networks show that the system achieves state-of-the-art accuracy in egomotion estimation tasks with event-based cameras, making it a promising solution for real-time, power-constrained robotics applications.

Index Terms—event-based vision, visual-odometry, neuromorphic computing, on-chip, spiking neural networks

I. INTRODUCTION

The estimation of egomotion plays an important role in applications such as autonomous navigation, robotics and Augmented Reality (AR). Conventionally, vehicle egomotion is determined using a combination of wheeled odometry and inertial sensing [1]. However, this approach has its limitations: wheeled odometry is unreliable on slippery terrain, and inertial sensors are prone to drift over long distances, leading to inaccurate motion estimation [2]. In contrast, Visual Odometry (VO) has emerged as a robust and accurate alternative, offering improved relative positioning and trajectory estimation. VO also provides a complementary data source that can be fused [3] with Inertial Measurement Unit (IMU) data to

maintain a reliable memory of an agent’s location within its environment [4, 5].

Typically VO relies on frame-based cameras, where the technology is mature and widely adopted. However, these systems often fail to meet the demands of high-speed, low-latency applications [6]. High-speed cameras generate large data streams, are energy-intensive, and require bulky hardware, all of which impose significant constraints on real-time processing, especially when deployed on vehicle payloads. To overcome these limitations, event-based vision sensors have emerged as an innovative alternative. Inspired by the biological retina, these sensors operate in an event-driven manner, capturing visual information with high temporal resolution and low-latency [7–9]. Their encoding of visual data, often as relative changes in luminance [9, 10], reduces power consumption and minimises redundant computation. This makes them well-suited for applications requiring low-latency positional feedback, such as VO on board autonomous drones [11, 12]. However, event-based cameras produce a continuous stream of asynchronous data (events), presenting emerging challenges for processing. Much of the effort to address these challenges has been directed toward creating processing pipelines that match the accuracy of frame-based camera solutions. A widely adopted approach involves converting event streams into frame-like representations by aggregating events over uniform time windows [13–24]. These event-frames are then processed using Artificial Neural Network (ANN) pipelines, such as Convolutional Neural Networks (CNNs), much like frame-based camera data. However, this approach undermines the key advantages of event-based sensing, particularly its low-latency capability. The conversion to frames inherently reintroduces latency, negating the original benefits of the event-driven paradigm. To capitalise on the advantages of event-based sensors, it is crucial to adopt equally event-driven data processing methods [25–27]. This remains an underexplored area of research.

Recent advancements in neuromorphic computing have driven the development of dedicated event-based processors designed to handle the unique characteristics of event streams [29, 30]. These processors are optimised to preserve the high-speed, asynchronous nature of event readouts, making them well-suited for real-time or closed-loop applications. However, many existing architectures remain limited in their ability to fully leverage the temporal precision of events for feature extraction. Most rely heavily on conventional models such as Leaky Integrate and Fire (LIF) neurons, which, while

¹ Bio-Inspired Circuits and Systems (BICS) Lab, Zernike Institute for Advanced Materials, University of Groningen, Netherlands.

² Groningen Cognitive Systems and Materials Center (CogniGron), University of Groningen, Netherlands.

³ Neuronova Ltd., Italy.

⁴ Micro- and Nanoelectronic Systems (MNES), Technische Universität Ilmenau, Germany.

⁵ Asynchronous VLSI and Architecture Group, School of Engineering & Applied Science (SEAS), Yale University, CT, USA.

* Corresponding author: h.r.greatorex@rug.nl

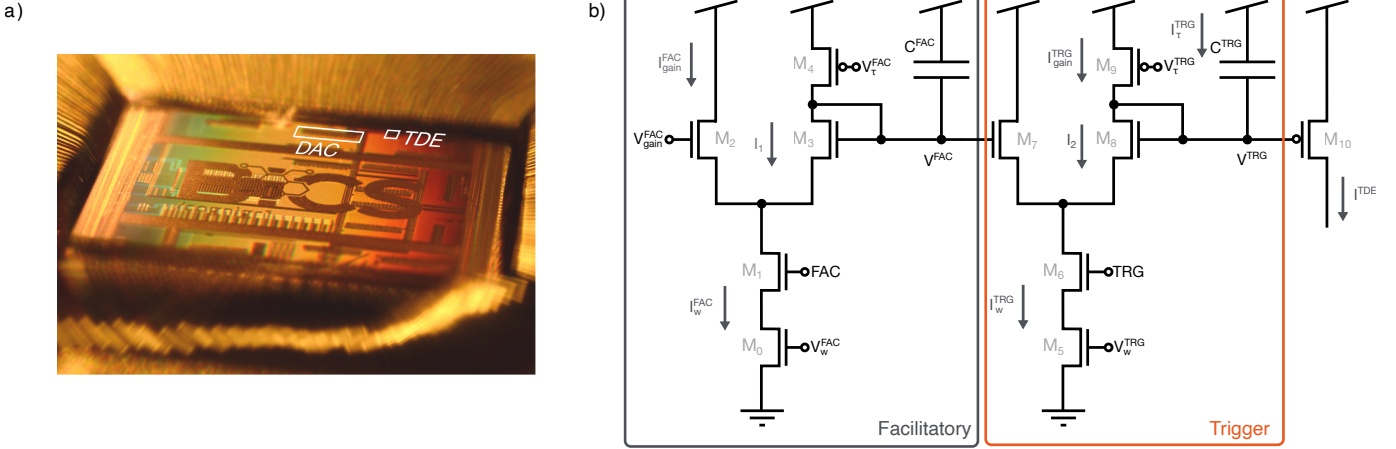


Fig. 1: Photograph of the *cognigr1* chip, fabricated in 180 nm technology along with the schematic of the TDE synapse. a) The relevant structures on the die are indicated. The total size of the TDE circuit is $19\mu\text{m}\times 56\mu\text{m}$ including guard rings and is biased by an on-chip DAC. b) Schematic of the state-of-the-art CMOS TDE synapse [28], with facilitatory and trigger blocks labeled.

widely used, are inadequate for capturing the richness of spike timing information in complex tasks, especially when embedded in shallow Spiking Neural Networks (SNNs). This highlights the growing demand for processing units capable of efficiently and robustly extracting meaningful spatiotemporal features from high-throughput event streams.

In this work, we present a fully event-based pipeline for egomotion estimation that uses precise event timing to extract optical flow from the asynchronous output of event-based cameras. Central to our approach is an on-chip implementation of the Time Difference Encoder (TDE) [31, 32], an event-based processing unit inspired by elementary motion detector circuits found in insect sensory pathways [33, 34]. The TDE converts the time differences between events on two input channels into an output event stream, capable of extracting spatiotemporal information from event-based data across various sensory domains [31, 32, 35–38]. In the event-vision domain, a layer of TDE elements is demonstrated in this work to provide a low-latency readout of egomotion. To validate the proposed pipeline, we conducted two complementary studies. We first applied an on-chip mixed-signal implementation of the TDE model to an egomotion reconstruction task, using a spatially-downsampled event stream captured by a car-mounted event camera in an urban environment. Then, we applied a scaled-up simulated network of TDE elements to the full dataset. The mixed-signal CMOS implementation demonstrates the viability of the approach for low-latency and energy-efficient operation, while the larger simulation highlights its scalability and suitability for real-world applications.

By avoiding frame-based intermediaries, our approach is well-suited for robotics tasks that demand real-time navigation on constrained power budgets. This advancement could enable more efficient and responsive autonomous systems, supporting future developments in low-latency, energy-constrained robotics [12, 39].

II. RESULTS

Here, we present the experimental validation and analysis of the TDE circuit [28] (Fig. 1), its application to an event-based egomotion estimation task when deployed in a lightweight SNN, and the results of scaling up the SNN in simulation. These simulations outperformed previous approaches in egomotion estimation accuracy across multiple dataset samples, demonstrating the scalability and robustness of the proposed network for real-world applications.

Time Difference Encoder Circuit

The TDE circuit [28] produces a subthreshold current (μA - nA), which inversely correlates with the time difference between two input events. This current is then integrated by a silicon LIF neuron [40, 41], producing output spikes with an instantaneous frequency also inversely correlated with the input time difference. This process utilizes two distinct integrator blocks, called *facilitatory* and *trigger*, collectively termed the TDE synapse, with each block receiving one of the two input channels of the TDE. Both integrator blocks initiate a time-decaying voltage trace in response to an event (or digital pulse). Upon arrival of an event at the Facilitatory (FAC) input, a decaying voltage trace is initiated. Concurrently, when an event arrives at the Trigger (TRG) input, a synaptic current is generated, with its amplitude proportional to the instantaneous value of the trigger trace relative to the power supply. This current is then integrated by a neuron circuit. The temporal proximity of FAC and TRG events determines the amplitude of the facilitatory trace at the arrival of the TRG spike and the subsequent Excitatory Postsynaptic Current (EPSC). As a result, the output spikes encode the input time difference through both their quantity and Interspike Interval (ISI). Thus, the TDE circuit functions as an asymmetric correlation detector, encoding the time difference between input events in an analog manner.

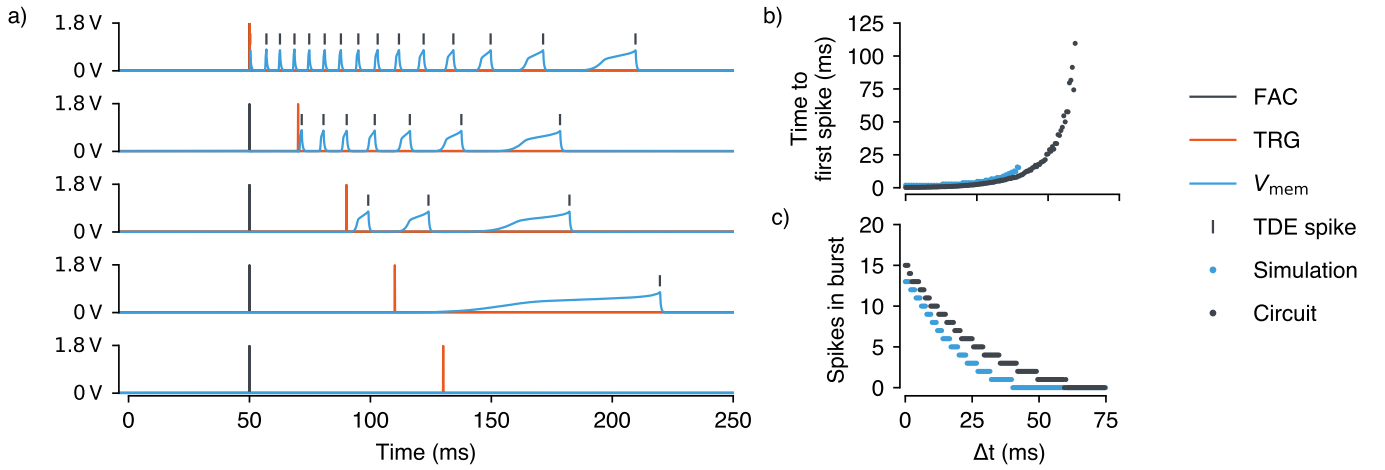


Fig. 2: Silicon measurements of the TDE circuit. **a)** The time (Δt) between FAC and TRG input events was increased systematically. Each plot shows a Δt increment of 20 ms from 0 ms to 80 ms. The membrane potential, V_{mem} of the neuron integrates the input current from the TDE synapse and outputs a spike when the threshold is reached. The encoding of the temporal distance between the input events is exhibited by the dynamics of V_{mem} and the associated output spikes of the TDE. **b)** The time to first spike of the TDE spiking output for increasing time difference between input events. The response of the simulated TDE model to the same input is also shown as a comparison. **c)** The number of spikes in the burst of the TDE with respect to the Δt of input events.

The instantaneous magnitude of the current sourced by the TDE synapse circuit, I^{TDE} , is proportional to the exponential of the time difference, Δt_{TDE} , between the FAC and TRG events. This relationship is also influenced by the time constant of the facilitatory block and is described by the following equation:

$$I^{\text{TDE}} \propto e^{-\frac{\Delta t_{\text{TDE}}}{\tau_{\text{FAC}}}} \quad (1)$$

The decay of this current, with this initial magnitude, is then described by:

$$I^{\text{TDE}}(t) \propto e^{-\frac{\Delta t_{\text{TDE}}}{\tau_{\text{FAC}}}} e^{-\frac{t}{\tau_{\text{TRG}}}} \quad (2)$$

This confirms that the circuit’s dynamics reflect the behaviour of the TDE simulation model (Supplementary S1). Specifically, there is an exponential relationship between Δt_{TDE} and the initial magnitude of the current injected into the spiking neuron.

TDE circuit measurements

The response of the TDE circuit to controlled input events was measured. In all experiments, the circuit was biased using the configurable on-chip Digital-to-Analog Converter (DAC). Fig. 2a shows the circuit’s response to a sweep of input events during which the time difference, Δt , between FAC and TRG events was incremented from 0 to 80 ms. The membrane potential, V_{mem} , and spiking output of the TDE are shown. It is evident that the circuit not only encodes the temporal separation of input events in the number of output spikes but also their relative timing within the burst. Fig. 2b and Fig. 2c more explicitly plot this relationship, exemplifying how the TDE circuit translates a temporal correlation into a burst of spikes (or events). Additionally, the behaviour of the simulated TDE model to the same input events is also shown, demonstrating the fidelity between the circuit and simulation

model. The parametrisation of the circuit and simulated model were not optimised for a specific task but chosen to have high spiking dynamic range over a Δt of 50 ms (parameters listed in Supplementary Table S2a and Table S2b).

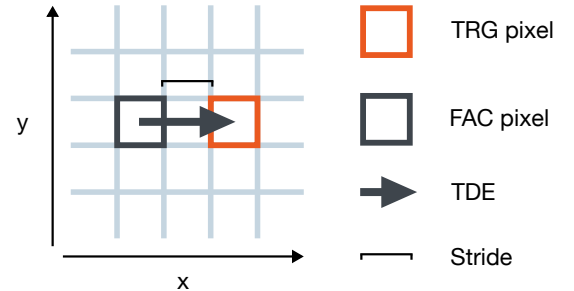


Fig. 3: The TDE can be applied to event-based vision tasks by “connecting” the FAC and TRG inputs to specific (x, y) pixels. In this way the TDE becomes receptive to a particular direction of motion. In this case the TDE is sensitive to left-right motion, indicated by the arrow representing the TDE connectivity. We define the stride as the pixel-wise separation of FAC and TRG inputs, in this example it is 1.

On-chip egomotion network emulation

To apply the TDE circuit to an event-based vision task, it is essential to establish some foundational intuition. The model is designed to process pairs of events through its two inputs. Conceptually, we can imagine “connecting” a single TDE unit to two pixels of an event-based camera sensor, with each FAC and TRG input corresponding to a specific (x, y) coordinate, or the events generated at that location. When configured this way, the TDE becomes sensitive to motion in a direction determined by the relative orientation of its FAC and TRG inputs within the (x, y) coordinates of the sensor (Fig. 3). By employing a population of TDE units,

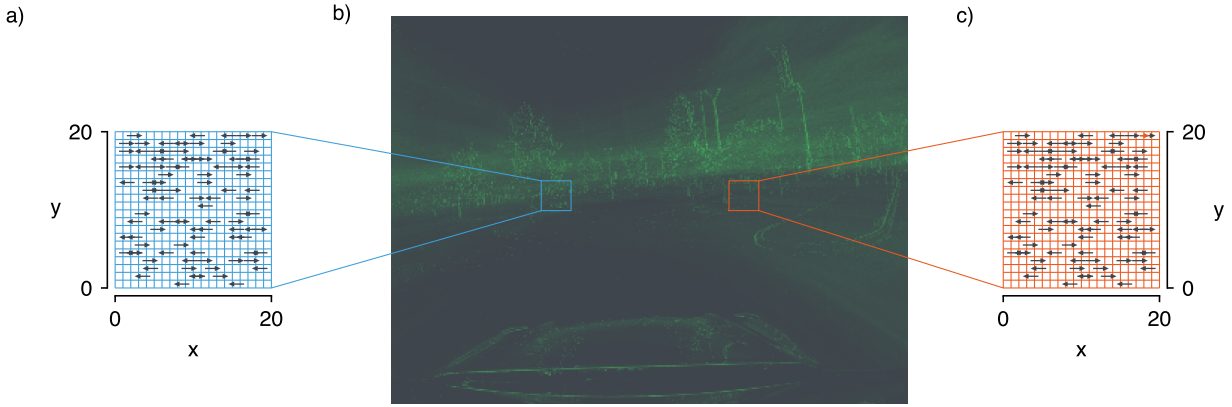


Fig. 4: An illustration of how the FAC and TRG connections are oriented for each TDE unit in relation to the (x, y) event data from the event camera. b) A single frame (generated by integrating activity over an arbitrary time step) of the MVSEC sample *outdoor_day1*. This event data was recorded by a DAVIS 346B Dynamic Vision Sensor (DVS) camera (346×260 pixels) situated on the bonnet of a vehicle driving through a city. The two boxes illustrate the two sample areas from which events were sampled to estimate the egomotion of the vehicle. Both boxes, **a)** and **c)**, referred to as left and right, are 20×20 pixels in size and contain 100 randomly placed TDEs, with an equal proportion orientated with either left-right or right-left polarity and a stride of 2 pixels. Both sample boxes have precisely the same placement of TDEs.

it is possible to construct a network receptive to particular motion directions across the visual field. Using the on-chip TDE model, one can emulate such a network by sequentially providing the appropriate event-based data and measuring the circuit’s response. As a proof of concept, this was able to be implemented with a single on-chip circuit, as the network operates in a purely feed-forward manner.

For this task, an SNN comprising of 200 TDE units was used. The TDEs were distributed within the visual field, as depicted in Fig. 4 and were positioned to be sensitive to the vehicle’s yaw rate, or, in other words, its turning velocity. Fig. 5 shows the IO events of the network emulated on-chip. Input data from the MVSEC [13] sample *outdoor_day1* is shown for both boxes positioned within the visual field (Fig. 4), along with the spiking response of the TDE populations. The estimated egomotion signal was generated by integrating the TDE spiking activity and computing the difference between the right-left and left-right oriented TDEs. This process was applied to both boxes, and the activity differences for each box were summed. The resulting signal was then normalised to the maximum absolute value over the duration of the sample. Fig. 6 displays the output of the on-chip network, the IMU recording and vehicle ground truth. The ground truth was generated using a fusion of LiDAR, IMU, motion capture, and GPS data [13]. The egomotion signal representing the yaw rate of the vehicle ($\dot{\psi}$) was measured with an Average Relative Rotational Error (ARRE) (Supplementary S2) of 0.00014 rad on-chip. As a comparison, the same network configuration with the same input events was simulated using the SNN simulator *Brian2*, demonstrating high similarity between the TDE simulation model and its circuit implementation.

On-chip network power consumption

We measured the power consumption of the TDE circuit while sequentially executing the network. A histogram of the

average power consumption per TDE over the duration of the event-camera sample is shown in Fig. 6c. A mean power consumption per TDE of 914 pW was measured. Therefore, when scaled by the number of units used in the network emulated on-chip (Fig. 5), a total power consumption of 1.8 nW is estimated for the TDEs in the network when performing the task. However, it is important to note that if such a system were fully realised in hardware, there would be additional power overhead associated with aggregating spiking activity to provide a readout of egomotion, as this process was performed off-chip in this work.

Scaled-up simulations

To assess the full-scale performance of the egomotion network, its size was increased. With the limitation of only a single TDE circuit on the *cognigr1* die these networks were run in simulation using the TDE model. While the network emulated on-chip was limited to receiving sparse input from two locations in the visual field, the full-scale network densely sampled the entire visual field, amounting to 178,880 TDE units in total (compared to 200 in the network emulated on-chip). This is comparable to the quantity of spiking neurons available on several cores of state-of-the-art neuromorphic processors. [42]. An identical approach of integrating the activity of left-right and right-left orientated TDE units and evaluating their difference in activity was applied. The results of these simulations are shown in Fig. 7, again with comparison against the IMU and ground truth. It is noted that in three cases (*outdoor_day1*, *outdoor_night2*, and *outdoor_night3*) the accumulated heading direction, ψ , suffers from less drift than the signal derived from the IMU when compared to the ground truth. The ARRE of the egomotion estimation for each sample, shown in Table I, highlights an improvement of at least one order of magnitude over previous works using the same dataset. The proposed network achieves

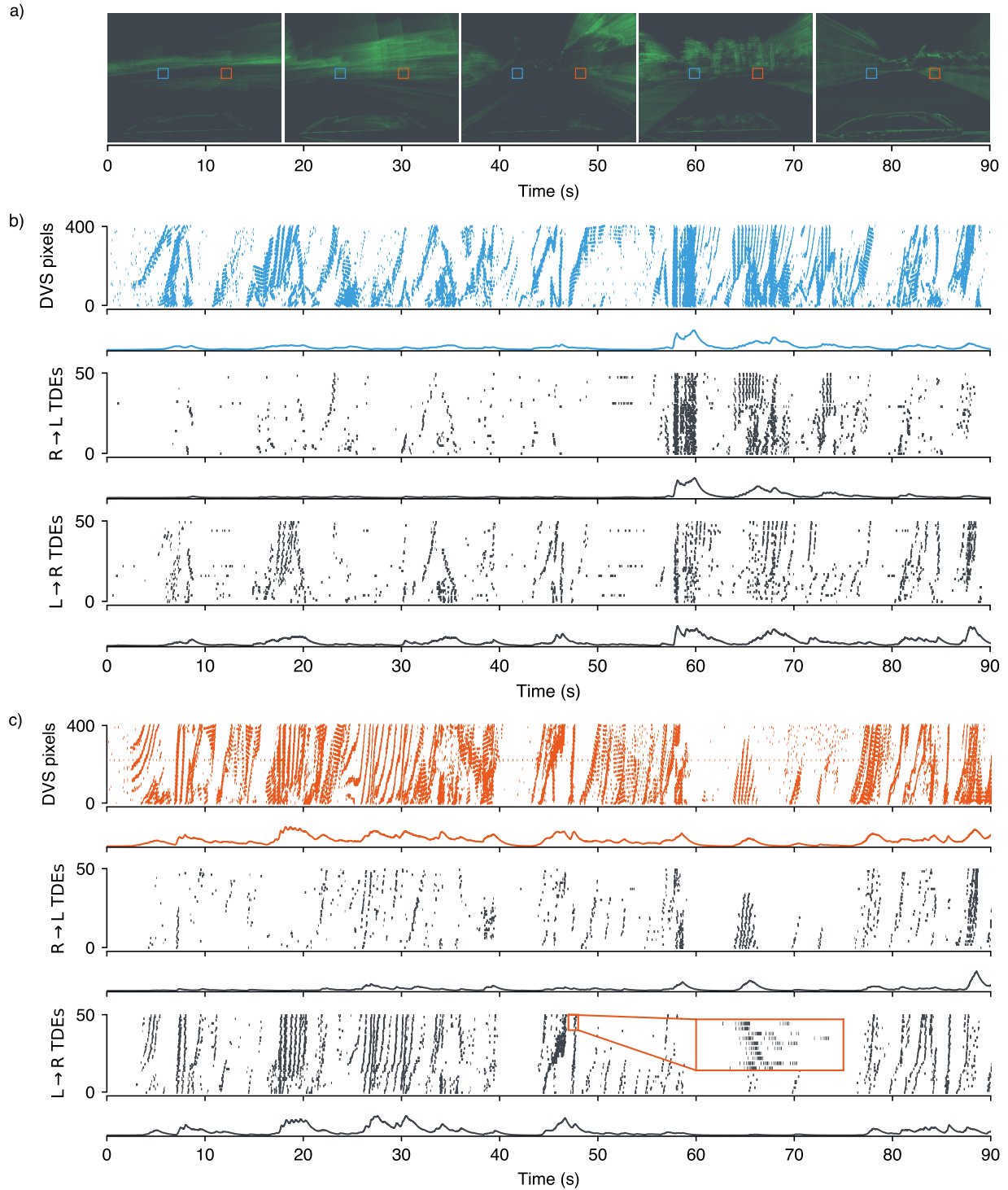


Fig. 5: Measurements from the TDE circuit on the *cognigr1* chip, implementing the egomotion estimation task. For this task the first 90 seconds of events from the *outdoor_day1* MVSEC sample were used. **a)** The event data from the event-camera mounted on the driving car. The two boxes (each 20×20 pixels) depict the two areas of the visual field from which events were sampled. **b)** The input events from the left box (blue) and the response of TDEs in the network orientated in the right-left ($R \rightarrow L$) and left-right ($L \rightarrow R$) direction. Below each raster plot the integrated activity, normalised for each box, is shown. This activity shows the differing sensitivity of TDE orientation and the event rate propagated through the network. **c)** The same information for the right box (orange). Additionally, a zoomed in section of the TDE network response is displayed to show the bursting activity of individual TDE units.

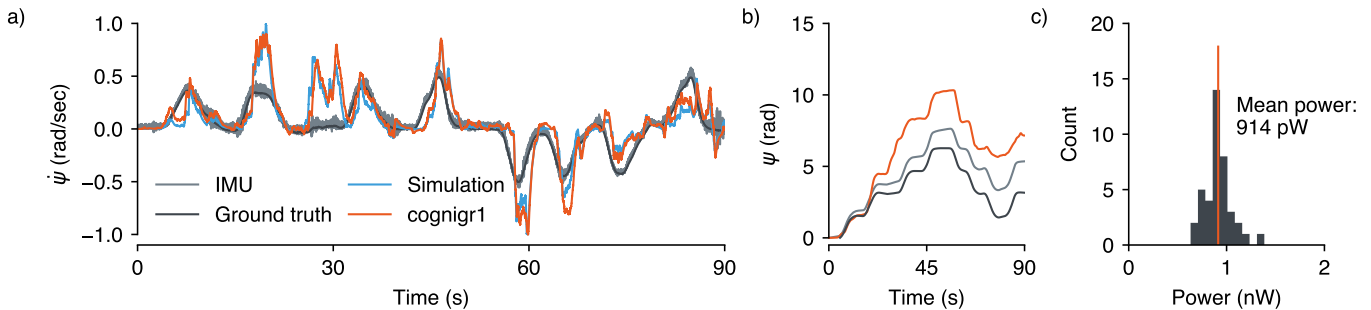


Fig. 6: **The egomotion estimation of the vehicle using the *cognigr1* chip.** **a)** The egomotion network activity compared with the IMU measurements from the vehicle and the recorded ground truth. The estimated motion is the angular velocity of the car, $\dot{\psi}$, as it turns, otherwise known as the yaw. The network activity plotted is from both on-chip measurements and *Brian2* simulations with exactly the same connectivity and input events. An ARRE of 0.000 14 rad is reported for both the simulated and on-chip network over the duration of the sample. **b)** The accumulated heading direction of the vehicle, ψ , constructed by integrating $\dot{\psi}$. **c)** On-chip power measurements of the TDE circuitry while performing the egomotion task, the average power consumption was measured for 40 random TDE instances within the emulated network. An average power consumption of 914 pW is reported per TDE in the network.

consistently lower error across all samples, demonstrating its effectiveness in enhancing egomotion estimation accuracy.

III. DISCUSSION

In this work, we leveraged event-based vision and processing within the event-based domain to enable accurate egomotion estimation, optimised for ultra-low power operation. Unlike current methods that convert event streams into frames for processing [17, 43–45], our method remains entirely event-based, enabling a significant reduction in latency and power consumption when executed on dedicated neuromorphic hardware. Notably, self-motion reconstruction in this work outperformed comparable event-framing-based approaches (Table I). A key strength of our approach lies in its simplicity and generalizability; the proposed network architecture does not rely on parameter optimisation or learning [46–48], making it robust to diverse and novel visual inputs. This contrasts with learning-based methods, especially those using CNNs, which often encounter difficulties in transferring across different domains and datasets. Such approaches are also particularly fragile when processing scenes consisting of independently moving objects. In this context, the configuration of the TDE units’ receptive fields, spatial distributions, and parameterisation required minimal engineering, leaving ample room for future exploration and optimisation. Despite the lack of optimisation, the results of our lightweight and shallow network architecture highlight the inherent effectiveness of our approach.

The network was validated through emulation on a custom mixed-signal subthreshold Integrated Circuit (IC), achieving competitive results against both IMU-based reconstructions and state-of-the-art event-based VO techniques. Despite sampling less than 1% of the visual field, the on-chip method accurately reconstructed self-motion all while consuming an estimated 1.8 nW. When scaled to the full visual field, simulations suggest that a hardware implementation of a TDE network on-chip could operate at a power budget of approximately 200 μ W, making it highly suitable for power-constrained applications such as micro-drones, edge comput-

ing devices, and Virtual Reality (VR) headsets [49]. A significant advantage of the proposed pipeline is its resource-efficient structure, as it eliminates the need for pre-processing steps like hot-pixel removal or spatiotemporal down-sampling [35, 50]. The potential for direct integration with event-based sensors would streamline the pipeline, aligning with advancements in custom asynchronous Application-Specific Integrated Circuits (ASICs) designed for event-driven architectures [30, 51]. Such integration further reinforces the feasibility of real-time, fully event-based processing pipelines in robotics systems [32, 39].

A comparative analysis with IMU-based heading direction systems revealed instances where our event-based network outperformed the IMU, particularly in scenarios where drift impacted inertial data. This suggests that our approach could augment IMU-based systems by recalibrating allocentric maps in real-time using visual inputs, particularly in GPS-denied environments. The capacity to leverage visual information in such scenarios highlights the broader utility of event-based egomotion estimation for maintaining robust and accurate navigation. Finally, the low-power consumption and efficient spike-timing-based processing of our approach make it particularly advantageous for platforms that require low-latency feedback on stringent energy constraints. Applications such as VR headsets or micro-drones, where power budgets are heavily limited, could benefit from the sparsification of computation enabled by this method. By addressing the dual challenges of latency and energy efficiency, this work offers a compelling alternative to traditional approaches, offering a promising solution for next-generation, low-power, real-time VO systems.

IV. METHODS

TDE circuit working principle

The first circuit implementation of the TDE model was previously proposed and tested in [31]. In this work, we introduce a modified version of the synaptic circuit [28] that employs two Differential Pair Integrator (DPI) circuits [52] to

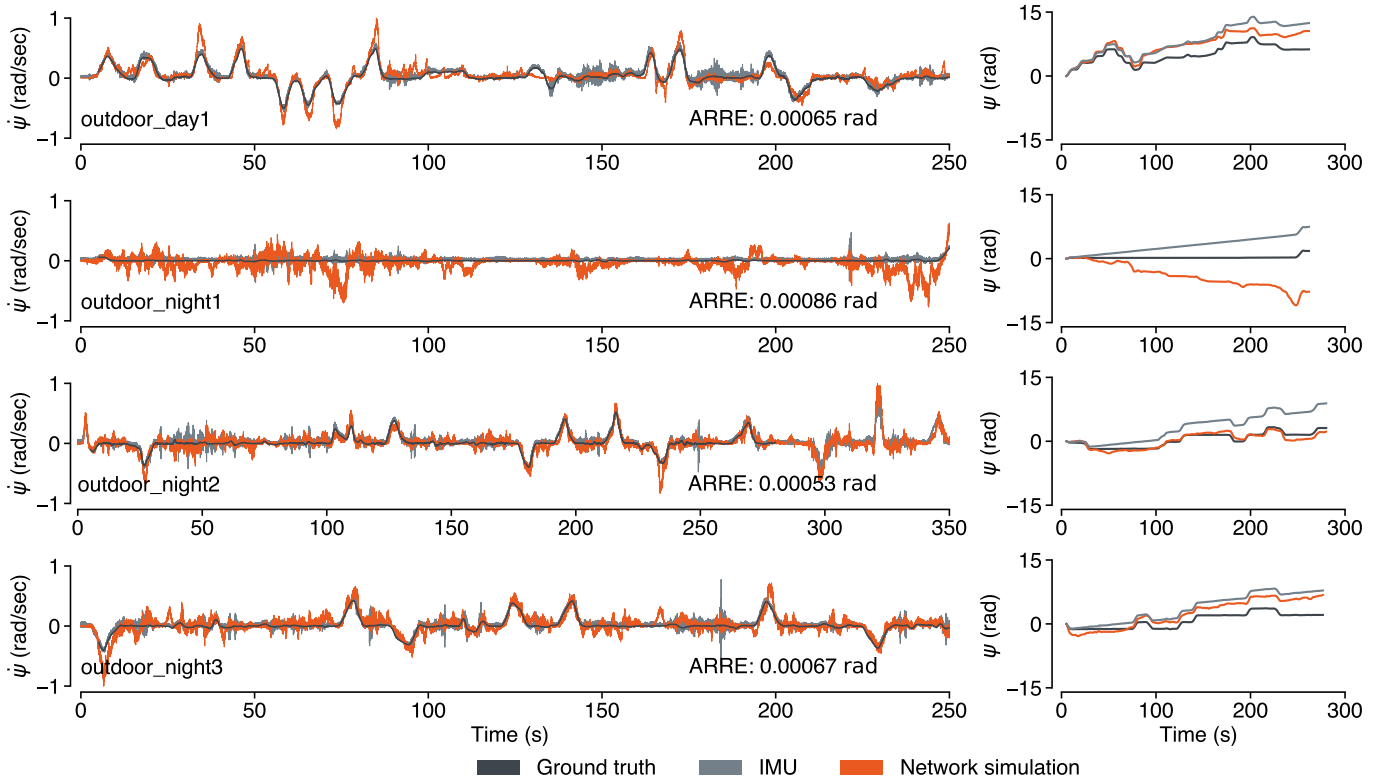


Fig. 7: The simulated scaled-up egomotion network sampling from the entire visual field. The network estimation is compared to the IMU recording and ground truth. The ARRE compared to the ground truth is reported for each driving sequence and the accumulated heading direction, ψ , is compared to the ground truth value and the value derived from the on-board IMU.

Comparison	ARRE (rad)			
	outdoor_day1	outdoor_night1	outdoor_night2	outdoor_night3
This work	0.00065	0.00086	0.00053	0.00067
[43]	0.0994	0.0632	0.116	0.121
[44] (SfMLearner [17])	0.00916	0.00433	0.00499	0.00482
[44]	0.00267	0.00139	0.00202	0.00202
[45]	0.00867	-	-	-

Table 1: Comparisons of the egomotion network in this work with other works estimating egomotion using the same dataset.

integrate FAC and TRG inputs on their respective tails. Similar to the algorithmic model, the CMOS implementation consists of a circuit for both the TDE synapse and the spiking neuron. The schematic for the TDE synapse is shown in Fig. 1b and the neuron schematic is shown in Supplementary Fig. S1, both circuits were realised using Metal Oxide Semiconductor (MOS) technology and operate in the subthreshold regime.

When an event (digital pulse) arrives at the FAC transistor, the tail of the first DPI drains charge from the capacitor C^{FAC} (fabricated as a MOS Capacitor (MOSCAP)). The magnitude of discharge is determined by the biases V_w^{FAC} and $V_{\text{gain}}^{\text{FAC}}$ (Supplementary S1). The capacitor C^{FAC} then recharges at a rate determined by the bias V_{τ}^{FAC} , thus raising the voltage V^{FAC} to V_{dd} with a time constant, τ_{FAC} . If, within this facilitation time, a TRG event arrives at the tail of the second DPI the voltage on the gate of transistor M_7 is sufficient to elicit the discharge of capacitor C^{TRG} . This magnitude of this discharge

is determined not only by the time since FAC events but also by the bias V_w^{TRG} . In a similar way, the TRG capacitor recharges at a rate determined by the bias V_{τ}^{TRG} , thus whilst the voltage V^{TDE} is below V_{dd} a current is conveyed through p-type MOS (pMOS) transistor M_{10} . The LIF circuit that integrates this current, I^{TDE} , elicits spiking activity, provided the current dynamics and neuron biasing are adequate. The neuron circuit fabricated in this work was derived from the DPI neuron first introduced in [41] and its behaviour is explained more comprehensively in Supplementary Fig. S1.

The aforementioned circuits were fabricated using the 180 nm X-FAB process on the *cognigr1* ASIC. The chip includes a single TDE and an on-chip 12-bit DAC, which supplies the subthreshold voltage parameters necessary for biasing the circuitry. To enable power measurements, the power supply of the TDE circuitry is isolated. A photograph of the fabricated chip is provided in Fig. 1a, highlighting the

approximate location of the circuits on the die.

TDE simulation model

The simulated TDE model has two inputs: Facilitatory (FAC) and Trigger (TRG), both of which receive events. The FAC input events are integrated onto the trace I_{FAC} , with dynamics given by

$$\frac{dI_{\text{FAC}}}{dt} = -\frac{I_{\text{FAC}}}{\tau_{\text{FAC}}} + \sum_i w^{\text{FAC}} \delta(t - t_i^{\text{FAC}}) \quad (3)$$

where τ_{FAC} is the time constant of the decay, $\delta(t - t_i^{\text{FAC}})$ is a FAC input event at time t_i^{FAC} , and w^{FAC} is a fixed weight. The TRG input events are similarly integrated, but the effective weight of the TRG spikes is determined by the value of the FAC trace,

$$\frac{dI_{\text{TRG}}}{dt} = -\frac{I_{\text{TRG}}}{\tau_{\text{TRG}}} + I_{\text{FAC}}(t) \sum_i w^{\text{TRG}} \delta(t - t_i^{\text{TRG}}) \quad (4)$$

where τ_{TRG} is the time constant of the decay, $\delta(t - t_i^{\text{TRG}})$ is a TRG input spike at time t_i^{TRG} , w^{TRG} a fixed weight, and $I_{\text{FAC}}(t)$ the value of the FAC trace at time t . The TRG trace is then treated as an EPSC into a LIF neuron with time constant τ_m and firing threshold u_θ , modeled as

$$\frac{du}{dt} = -\frac{u}{\tau_m} + I_{\text{TRG}} \quad (5)$$

where u is the neuron's membrane potential. When u exceeds the firing threshold u_θ , a spike is produced and u is reset to 0. This system of coupled ODEs was simulated in discrete time steps using the Euler method.

Egomotion network

A population of TDE units was assembled across the visual field, with FAC and TRG connectivity configured to be sensitive to motion. As illustrated in Fig. 3, the FAC and TRG inputs can be mapped to the pixels from an event camera, in this example, the TDE unit is sensitive to left-right motion and has a stride of 1: corresponding to the number of pixels separating the two inputs.

The motion of static objects in a scene due to self-motion can be discerned by a network of TDE units. In this way, the mapping of a population of TDEs can be chosen arbitrarily or selected specifically to be receptive to certain degrees of motion across the entire visual field or segments of it. In this work, the orientations of TDE units were chosen to be either right-left or left-right sensitive. These orientations are therefore primarily receptive to the motion of an agent moving relative to its yaw axis, in other words, left and right turns. The output spikes of each population of TDEs, corresponding to the two opposing orientations, were integrated to provide an estimate of the motion in their preferred direction. This integration was modeled as a leaky integrator where events from left-right orientated TDEs, $\delta(t - t_i^{L \rightarrow R})$, increment the activity variable, A , and right-left events, $\delta(t - t_i^{R \rightarrow L})$, decrement it. The time constant of this process is given by τ_A .

$$\tau_A \frac{dA}{dt} = -A + \sum_i \delta(t - t_i^{L \rightarrow R}) - \sum_i \delta(t - t_i^{R \rightarrow L}) \quad (6)$$

This relative activity of the two populations was then normalised with a normalisation constant determined by the absolute maximum activity for the duration of the sample. All experiments and simulations described in the preceding sections used the MVSEC dataset as input event data. Events of both polarities from a single event camera (the left camera in the stereoscopic setup) and its IMU were used.

1) *On-chip*: A single TDE circuit is realised on the *cognigr1* ASIC, therefore the network was run serially in time. The network has a feed-forward architecture therefore the response of each TDE could be tested in isolation and the network could be executed sequentially. Given this constraint and the large number of pixels within the visual field available to be sampled from, a spatially downsampled network configuration was deployed. Fig. 4 illustrates the setup for the egomotion network that was executed on-chip. Two sample areas were chosen to be 20×20 in size, referred to as left and right boxes. Both boxes were positioned in the vertical center of the visual field but offset in the x -direction by 100 pixels ($\sim 30\%$ from the center). Within each box, a population of 100 TDE units of half left-right orientation and half right-left orientation was randomly distributed with a stride of 2 pixels, this distribution was identical for both boxes (Fig. 4a,c). This configuration was chosen arbitrarily to process a reasonable subspace of the input events, excluding, for example, events generated by the car's bonnet. Within each box, the differential activity (Eq.6) of the opposing TDE orientations was computed and then summed for both boxes, resulting in a signal representative of the self-motion of the vehicle. For the on-chip experiments, the biasing of the TDE circuitry was fixed, these biases are listed in Table S2a. Additionally, the power consumption of the isolated TDE and neuron circuit was measured for a random 40 runs using an Source Measurement Unit (SMU). The identical network configuration with the same input data was also simulated using the *Brian2* simulator [53], the parameters of this simulation are provided in Table S2b.

2) *Simulation*: To analyse the effect of scaling up the egomotion network—an approach unfeasible due to the spatial resolution of state-of-the-art event cameras and the limitation of a single TDE circuit on the chip—it was simulated in discrete time on a Graphics Processing Unit (GPU) using the *JAX* library. This approach enabled dense sampling of the entire visual field, as illustrated in Fig. 4b, and allowed for egomotion estimation to be obtained as if a large array of TDE units were implemented on-chip. This network utilised 178,880 units with an equal split of each TDE orientation and a stride of 2 pixels. The TDE model parameters used in these simulations are provided in Supplementary Table S2c.

V. ACKNOWLEDGMENTS

This work has been supported by DFG projects MemTDE (441959088) and NMVAC (432009531), and EU H2020 projects NeuTouch (813713). Funded by the Deutsche Forschungsgemeinschaft (DFG German Research Foundation) - Project number 432009531. O.R. and M.M. were solely

affiliated with BICS¹ and CogniGron² during the time of this work. The authors would like to acknowledge the financial support of the CogniGron research center and the Ubbo Emmius Funds (Univ. of Groningen). The authors would also like to acknowledge Philipp Klein and Ton Juny Pina for soldering the PCBs.

VI. CONTRIBUTIONS

Conceptualisation - H. G., E.C.; Methodology - H. G., M. C., M. M., O. R., E.C.; Software/Hardware - H. G., M. M., O. R.; Investigation - H. G., M. M., E.C.; Writing - H. G., M. C., M. M., O. R., E.C.; Visualisation - H. G., M. C.; Supervision - E. C.

REFERENCES

- [1] J. Borenstein, H. R. Everett, L. Feng, and D. Wehe, “Mobile robot positioning: Sensors and techniques”, *Journal of Robotic Systems*, vol. 14, no. 4, pp. 231–249, 1997. DOI: 10.1002/(SICI)1097-4563(199704)14:4<231::AID-ROB2>3.0.CO;2-R.
- [2] D. Scaramuzza and F. Fraundorfer, “Visual Odometry [Tutorial]”, *IEEE Robotics & Automation Magazine*, vol. 18, no. 4, pp. 80–92, 2011. DOI: 10.1109/MRA.2011.943233.
- [3] E. Mueggler, G. Gallego, H. Rebecq, and D. Scaramuzza, “Continuous-Time Visual-Inertial Odometry for Event Cameras”, *IEEE Transactions on Robotics*, vol. 34, no. 6, pp. 1425–1440, 2018. DOI: 10.1109/TRO.2018.2858287.
- [4] D. Nister, O. Naroditsky, and J. Bergen, “Visual odometry,” in *Proceedings of the 2004 IEEE Computer Society Conference on Computer Vision and Pattern Recognition, 2004. CVPR 2004.*, vol. 1, 2004, pp. I–I. DOI: 10.1109/CVPR.2004.1315094.
- [5] D. Nistér, O. Naroditsky, and J. Bergen, “Visual odometry for ground vehicle applications”, *Journal of Field Robotics*, vol. 23, no. 1, pp. 3–20, 2006. DOI: 10.1002/rob.20103.
- [6] D. Gehrig and D. Scaramuzza, “Low-latency automotive vision with event cameras”, *Nature*, vol. 629, no. 8014, pp. 1034–1040, 2024. DOI: 10.1038/s41586-024-07409-w.
- [7] M. Mahowald, “The Silicon Retina”, *An Analog VLSI System for Stereoscopic Vision*, pp. 4–65, 1994. DOI: 10.1007/978-1-4615-2724-4_2.
- [8] C. A. Mead and M. A. Mahowald, “A silicon model of early visual processing”, *Neural Networks*, vol. 1, no. 1, pp. 91–97, 1988. DOI: 10.1016/0893-6080(88)90024-X.
- [9] P. Lichtsteiner, C. Posch, and T. Delbruck, “A 128 × 128 120 dB 15 μs latency asynchronous temporal contrast vision sensor”, *IEEE Journal of Solid-State Circuits*, vol. 43, no. 2, pp. 566–576, 2008. DOI: 10.1109/JSSC.2007.914337.
- [10] C. Posch, D. Matolin, and R. Wohlgenannt, “A QVGA 143 dB dynamic range frame-free PWM image sensor with lossless pixel-level video compression and time-domain CDS”, *IEEE Journal of Solid-State Circuits*, vol. 46, no. 1, pp. 259–275, 2011. DOI: 10.1109/JSSC.2010.2085952.
- [11] G. Chen, H. Cao, J. Conrath, H. Tang, F. Rohrbein, and A. Knoll, “Event-Based Neuromorphic Vision for Autonomous Driving: A Paradigm Shift for Bio-Inspired Visual Sensing and Perception”, *IEEE Signal Processing Magazine*, vol. 37, no. 4, pp. 34–49, 2020. DOI: 10.1109/MSP.2020.2985815.
- [12] E. Kaufmann, L. Bauersfeld, A. Loquercio, M. Müller, V. Koltun, and D. Scaramuzza, “Champion-level drone racing using deep reinforcement learning”, *Nature*, vol. 620, no. 7976, pp. 982–987, 2023. DOI: 10.1038/s41586-023-06419-4.
- [13] A. Z. Zhu, L. Yuan, K. Chaney, and K. Daniilidis, “EV-FlowNet: Self-Supervised Optical Flow Estimation for Event-based Cameras”, *Robotics: Science and Systems*, 2018. DOI: 10.15607/RSS.2018.XIV.062.
- [14] U. M. Nunes and Y. Demiris, “Robust Event-Based Vision Model Estimation by Dispersion Minimisation”, *IEEE Transactions on Pattern Analysis and Machine Intelligence*, vol. 44, no. 12, pp. 9561–9573, 2022. DOI: 10.1109/TPAMI.2021.3130049.
- [15] C. Lee, A. K. Kosta, A. Z. Zhu, K. Chaney, K. Daniilidis, and K. Roy, “Spike-FlowNet: Event-Based Optical Flow Estimation with Energy-Efficient Hybrid Neural Networks”, *Lecture Notes in Computer Science*, vol. 12374 LNCS, pp. 366–382, 2020. DOI: 10.1007/978-3-030-58526-6_22/COVER.
- [16] J. Cuadrado, U. Rançon, B. R. Cottreau, F. Barranco, and T. Masquelier, “Optical flow estimation from event-based cameras and spiking neural networks”, *Frontiers in Neuroscience*, vol. 17, p. 1160034, 2023. DOI: 10.3389/FNINS.2023.1160034/BIBTEX.
- [17] T. Zhou, M. Brown, N. Snavely, and D. G. Lowe, “Unsupervised Learning of Depth and Ego-Motion From Video,” in *Proceedings of the IEEE Conference on Computer Vision and Pattern Recognition*, 2017, pp. 1851–1858.
- [18] A. Censi and D. Scaramuzza, “Low-latency event-based visual odometry”, *Proceedings - IEEE International Conference on Robotics and Automation*, pp. 703–710, 2014. DOI: 10.1109/ICRA.2014.6906931.
- [19] A. Vitale, A. Renner, C. Nauer, D. Scaramuzza, and Y. Sandamirskaya, “Event-driven Vision and Control for UAVs on a Neuromorphic Chip”, *Proceedings - IEEE International Conference on Robotics and Automation*, vol. 2021-May, pp. 103–109, 2021. DOI: 10.1109/ICRA48506.2021.9560881.
- [20] A. Mitrokhin, C. Fermuller, C. Parameshwara, and Y. Aloimonos, “Event-Based Moving Object Detection and Tracking”, *IEEE International Conference on Intelligent Robots and Systems*, pp. 6895–6902, 2018. DOI: 10.1109/IROS.2018.8593805.
- [21] A. Mitrokhin, C. Ye, C. Fermüller, Y. Aloimonos, and T. Delbruck, “EV-IMO: Motion Segmentation Dataset and Learning Pipeline for Event Cameras,” in *2019 IEEE/RSJ International Conference on Intelligent Robots and Systems (IROS)*, 2019, pp. 6105–6112. DOI: 10.1109/IROS40897.2019.8968520.
- [22] G. Gallego, J. E. A. Lund, E. Mueggler, H. Rebecq, T. Delbruck, and D. Scaramuzza, “Event-based, 6-DOF Camera Tracking from Photometric Depth Maps”, *IEEE Transactions on Pattern Analysis and Machine Intelligence*, vol. 40, no. 10, pp. 2402–2412, 2018. DOI: 10.1109/TPAMI.2017.2769655.
- [23] G. Gallego and D. Scaramuzza, “Accurate Angular Velocity Estimation With an Event Camera”, *IEEE Robotics and Automation Letters*, vol. 2, no. 2, pp. 632–639, 2017. DOI: 10.1109/LRA.2016.2647639.
- [24] A. Renner, L. Supic, A. Danielescu, G. Indiveri, E. P. Frady, F. T. Sommer, and Y. Sandamirskaya, “Visual odometry with neuromorphic resonator networks”, *Nature Machine Intelligence*, vol. 6, no. 6, pp. 653–663, 2024. DOI: 10.1038/s42256-024-00846-2.
- [25] R. Benosman, C. Clercq, X. Lagorce, S.-H. Ieng, and C. Bartolozzi, “Event-Based Visual Flow”, *IEEE Transactions on Neural Networks and Learning Systems*, vol. 25, no. 2, pp. 407–417, 2014. DOI: 10.1109/TNNLS.2013.2273537.
- [26] G. Haessig, A. Cassidy, R. Alvarez, R. Benosman, and G. Orchard, “Spiking Optical Flow for Event-Based Sensors Using IBM’s TrueNorth Neurosynaptic System”, *IEEE Transactions on Biomedical Circuits and Systems*, vol. 12, no. 4, pp. 860–870, 2018. DOI: 10.1109/TBCAS.2018.2834558.
- [27] A. Amir, B. Taba, D. Berg, T. Melano, J. McKinstry, C. Di Nolfo, T. Nayak, A. Andreopoulos, et al., “A Low Power, Fully Event-Based Gesture Recognition System,” in *Proceedings of the IEEE Conference on Computer Vision and Pattern Recognition*, 2017, pp. 7243–7252.

- [28] H. Greatorex, M. Mastella, O. Richter, M. Cotteret, W. S. Girão, E. Janotte, and E. Chicca, “A scalable event-driven spatiotemporal feature extraction circuit”, 2025. DOI: 10.48550/arXiv.2501.10155.
- [29] Y. Yang, A. Kneip, and C. Frenkel, “EvGNN: An Event-driven Graph Neural Network Accelerator for Edge Vision”, *IEEE Transactions on Circuits and Systems for Artificial Intelligence*, pp. 1–14, 2024. DOI: 10.1109/TCASAI.2024.3520905.
- [30] M. Yao, O. Richter, G. Zhao, N. Qiao, Y. Xing, D. Wang, T. Hu, W. Fang, *et al.*, “Spike-based dynamic computing with asynchronous sensing-computing neuromorphic chip”, *Nature Communications*, vol. 15, no. 1, p. 4464, 2024. DOI: 10.1038/s41467-024-47811-6.
- [31] M. B. Milde, O. J. N. Bertrand, H. Ramachandran, M. Egelhaaf, and E. Chicca, “Spiking Elementary Motion Detector in Neuromorphic Systems”, *Neural Computation*, vol. 30, no. 9, pp. 2384–2417, 2018. DOI: 10.1162/neco_a_01112.
- [32] T. Schoepe, E. Janotte, M. B. Milde, O. J. N. Bertrand, M. Egelhaaf, and E. Chicca, “Finding the gap: Neuromorphic motion-vision in dense environments”, *Nature Communications*, vol. 15, no. 1, p. 817, 2024. DOI: 10.1038/s41467-024-45063-y.
- [33] A. Borst and T. Euler, “Seeing Things in Motion: Models, Circuits, and Mechanisms”, *Neuron*, vol. 71, no. 6, pp. 974–994, 2011. DOI: 10.1016/J.NEURON.2011.08.031.
- [34] W. Reichardt, “Autokorrelations-Auswertung als Funktionssprinzip des Zentralnervensystems: (bei der optischen Bewegungswahrnehmung eines Insektes)”, *Zeitschrift für Naturforschung B*, vol. 12, no. 7, pp. 448–457, 1957. DOI: 10.1515/znb-1957-0707.
- [35] G. D’Angelo, E. Janotte, T. Schoepe, J. O’Keefe, M. B. Milde, E. Chicca, and C. Bartolozzi, “Event-Based Eccentric Motion Detection Exploiting Time Difference Encoding”, *Frontiers in Neuroscience*, vol. 14, 2020. DOI: 10.3389/fnins.2020.00451.
- [36] T. Schoepe, D. Gutierrez-Galan, J. P. Dominguez-Morales, H. Greatorex, A. Jimenez-Fernandez, A. Linares-Barranco, and E. Chicca, “Closed-loop sound source localization in neuromorphic systems”, *Neuromorphic Computing and Engineering*, vol. 3, no. 2, 2023. DOI: 10.1088/2634-4386/ACDABA.
- [37] T. Schoepe, D. Drix, F. M. Schüffny, R. Miko, S. Sutton, E. Chicca, and M. Schmuker, “Odour Localization in Neuromorphic Systems,” in *2024 IEEE International Symposium on Circuits and Systems (ISCAS)*, 2024, pp. 1–5. DOI: 10.1109/ISCAS58744.2024.10558186.
- [38] S. Chiavazza, S. M. Meyer, and Y. Sandamirskaya, “Low-Latency Monocular Depth Estimation Using Event Timing on Neuromorphic Hardware,” in *Proceedings of the IEEE/CVF Conference on Computer Vision and Pattern Recognition (CVPR) Workshops*, 2023, pp. 4071–4080.
- [39] F. Paredes-Vallés, J. J. Hagenars, J. Dupeyroux, S. Stroobants, Y. Xu, and G. C. H. E. de Croon, “Fully neuromorphic vision and control for autonomous drone flight”, *Science Robotics*, vol. 9, no. 90, eadi0591, 2024. DOI: 10.1126/scirobotics.adi0591.
- [40] P. Livi and G. Indiveri, “A current-mode conductance-based silicon neuron for address-event neuromorphic systems,” in *2009 IEEE International Symposium on Circuits and Systems*, 2009, pp. 2898–2901. DOI: 10.1109/ISCAS.2009.5118408.
- [41] E. Chicca, F. Stefanini, C. Bartolozzi, and G. Indiveri, “Neuromorphic Electronic Circuits for Building Autonomous Cognitive Systems”, *Proceedings of the IEEE*, vol. 102, no. 9, pp. 1367–1388, 2014. DOI: 10.1109/JPROC.2014.2313954.
- [42] G. Orchard, E. P. Frady, D. B. D. Rubin, S. Sanborn, S. B. Shrestha, F. T. Sommer, and M. Davies, “Efficient Neuromorphic Signal Processing with Loihi 2,” in *2021 IEEE Workshop on Signal Processing Systems (SiPS)*, Coimbra, Portugal, 2021, pp. 254–259. DOI: 10.1109/SiPS52927.2021.00053.
- [43] A. Mitrokhin, P. Sutor, C. Fermüller, and Y. Aloimonos, “Learning sensorimotor control with neuromorphic sensors: Toward hyperdimensional active perception”, *Science Robotics*, vol. 4, no. 30, 2019. DOI: 10.1126/scirobotics.aaw6736.
- [44] C. Ye, A. Mitrokhin, C. Fermüller, J. A. Yorke, and Y. Aloimonos, “Unsupervised learning of dense optical flow, depth and egomotion with event-based sensors”, *IEEE International Conference on Intelligent Robots and Systems*, pp. 5831–5838, 2020. DOI: 10.1109/IROS45743.2020.9341224.
- [45] A. Z. Zhu, L. Yuan, K. Chaney, and K. Daniilidis, “Unsupervised Event-Based Learning of Optical Flow, Depth, and Egomotion,” in *Proceedings of the IEEE/CVF Conference on Computer Vision and Pattern Recognition*, 2019, pp. 989–997.
- [46] M. Gehrig, M. Millhausler, D. Gehrig, and D. Scaramuzza, “E-RAFT: Dense Optical Flow from Event Cameras”, *Proceedings - 2021 International Conference on 3D Vision, 3DV 2021*, pp. 197–206, 2021. DOI: 10.1109/3DV53792.2021.00030.
- [47] F. Paredes-Vallés, K. Y. W. Scheper, C. De Wagter, and G. C. H. E. de Croon, “Taming Contrast Maximization for Learning Sequential, Low-latency, Event-based Optical Flow,” in *Proceedings of the IEEE/CVF International Conference on Computer Vision*, 2023, pp. 9695–9705.
- [48] S. Shiba, Y. Klose, Y. Aoki, and G. Gallego, “Secrets of Event-Based Optical Flow, Depth and Ego-Motion Estimation by Contrast Maximization”, *IEEE Transactions on Pattern Analysis and Machine Intelligence*, vol. 46, no. 12, pp. 7742–7759, 2024. DOI: 10.1109/TPAMI.2024.3396116.
- [49] D. Palossi, A. Loquercio, F. Conti, E. Flamand, D. Scaramuzza, and L. Benini, “A 64-mW DNN-Based Visual Navigation Engine for Autonomous Nano-Drones”, *IEEE Internet of Things Journal*, vol. 6, no. 5, pp. 8357–8371, 2019. DOI: 10.1109/IJOT.2019.2917066.
- [50] M. Yedutenko, F. Paredes-Valles, L. Khacef, and G. C. H. E. De Croon, “TDE-3: An improved prior for optical flow computation in spiking neural networks”, 2024. DOI: 10.48550/arXiv.2402.11662.
- [51] M. Lefebvre and D. Bol, “A Mixed-Signal Near-Sensor Convolutional Imager SoC with Charge-Based 4b-Weighted 5-to-84-TOPS/W MAC Operations for Feature Extraction and Region-of-Interest Detection,” in *2024 IEEE Custom Integrated Circuits Conference (CICC)*, 2024, pp. 1–2. DOI: 10.1109/CICC60959.2024.10528961.
- [52] C. Bartolozzi and G. Indiveri, “Synaptic Dynamics in Analog VLSI”, *Neural Computation*, vol. 19, no. 10, pp. 2581–2603, 2007. DOI: 10.1162/neco.2007.19.10.2581.
- [53] M. Stimberg, R. Brette, and D. F. Goodman, “Brian 2, an intuitive and efficient neural simulator”, *eLife*, vol. 8, e47314, 2019. DOI: 10.7554/eLife.47314.

SUPPLEMENTARY MATERIAL

S1. TDE SYNAPSE CIRCUIT ANALYSIS

The following section refers to Fig. 1b and the currents, capacitances and voltages shown on the schematic. This approach to characterise the behaviour of the TDE circuit is derived from similar analysis of DPI circuits found in literature [1]. In order to derive the dynamics of V^{FAC} , an expression for the current flow, I_1 , as a result of a digital pulse arriving at the gate transistor M_1 is required. The following assumes that the subthreshold slopes of the MOS transistors is the same for pMOS and n-type MOS (nMOS) transistors, $k_n \approx k_p \approx k$. The subthreshold currents through transistors M_2 and M_7 are given by the following equations.

$$I_{\text{gain}}^{\text{FAC}} = I_0 e^{-\frac{\kappa}{U_T} V_{\text{gain}}^{\text{FAC}}} \quad (1)$$

$$I_{\text{gain}}^{\text{TRG}} = I_0 e^{-\frac{\kappa}{U_T} V^{\text{FAC}}} \quad (2)$$

The current I_1 given by the behaviour of the DPI and the biasing of the circuit's transistors can be written and refactored as follows.

$$I_1 = I_w^{\text{FAC}} \frac{e^{\frac{\kappa V^{\text{FAC}}}{U_T}}}{e^{\frac{\kappa V^{\text{FAC}}}{U_T}} + e^{\frac{\kappa V_{\text{gain}}^{\text{FAC}}}{U_T}}} \quad (3)$$

$$I_1 = \frac{I_w^{\text{FAC}}}{1 + \frac{I_{\text{gain}}^{\text{TRG}}}{I_{\text{gain}}^{\text{FAC}}}} \quad (4)$$

The voltage V^{FAC} is determined by the movement of charge on capacitor C^{FAC} . These dynamics are governed by the following Differential Equation (DE), where I_{τ}^{FAC} is a constant leak controlled by the biasing of transistor M_4 , V_{τ}^{FAC} .

$$C^{\text{FAC}} \frac{d}{dt} V^{\text{FAC}} = (I_1 - I_{\tau}^{\text{FAC}}) \quad (5)$$

Additionally, the current flowing through pMOS transistor M_4 , operating in the threshold regime is given by the following equation.

$$I_{\tau}^{\text{FAC}} = I_0 e^{-\frac{\kappa}{U_T} (V_{\tau}^{\text{FAC}} - V_{\text{dd}})} \quad (6)$$

Taking the time derivative of equation 2 and equating with equation 8.

$$\frac{d}{dt} V^{\text{FAC}} = -\frac{1}{C^{\text{FAC}}} (I_1 - I_{\tau}^{\text{FAC}}) \quad (7)$$

$$\frac{d}{dt} V^{\text{FAC}} = -\frac{U_T}{\kappa} \frac{1}{I_{\text{gain}}^{\text{TRG}}} \frac{dI_{\text{gain}}^{\text{TRG}}}{dt} \quad (8)$$

$$\frac{dI_{\text{gain}}^{\text{TRG}}}{dt} = \frac{I_{\text{gain}}^{\text{TRG}} \kappa}{U_T C^{\text{FAC}}} (-I_1 - I_{\tau}^{\text{FAC}}) \quad (9)$$

Substituting I_1

$$\frac{dI_{\text{gain}}^{\text{TRG}}}{dt} = \frac{I_{\text{gain}}^{\text{TRG}} \kappa}{U_T C^{\text{FAC}}} \left(\frac{I_w^{\text{FAC}}}{1 + \frac{I_{\text{gain}}^{\text{TRG}}}{I_{\text{gain}}^{\text{FAC}}}} - I_{\tau}^{\text{FAC}} \right) \quad (10)$$

Collecting terms and defining τ_{FAC}

$$\tau_{\text{FAC}} \frac{dI_{\text{gain}}^{\text{TRG}}}{dt} = I_{\text{gain}}^{\text{TRG}} \left(\frac{1}{I_{\tau}^{\text{FAC}}} \frac{I_w^{\text{FAC}}}{1 + \frac{I_{\text{gain}}^{\text{TRG}}}{I_{\text{gain}}^{\text{FAC}}}} - 1 \right) \quad (11)$$

$$\tau_{\text{FAC}} = \frac{U_T C^{\text{FAC}}}{\kappa I_{\tau}^{\text{FAC}}} \quad (12)$$

If $I_w^{\text{FAC}} \gg I_{\text{FAC}\tau}$, then $I_{\text{gain}}^{\text{FAC}}$ will eventually rise to such that $I_{\text{gain}}^{\text{TRG}} \gg I_{\text{gain}}^{\text{FAC}}$, when the circuit is stimulated with a step signal. If $\frac{I_{\text{gain}}^{\text{TRG}}}{I_{\text{gain}}^{\text{FAC}}} \gg 1$ the $I_{\text{gain}}^{\text{TRG}}$ dependence in 11 cancels out.

$$\tau_{\text{FAC}} \frac{dI_{\text{gain}}^{\text{TRG}}}{dt} + I_{\text{gain}}^{\text{TRG}} = \frac{I_w^{\text{FAC}}}{I_{\text{FAC}\tau}} I_{\text{gain}}^{\text{FAC}} \quad (13)$$

The response of $I_{\text{gain}}^{\text{TRG}}$ arrive at FAC at t^- and ending at t^+ is

$$I_{\text{gain}}^{\text{TRG}}(t) = \begin{cases} \frac{I_w^{\text{FAC}} I_{\text{gain}}^{\text{FAC}}}{I_{\text{FAC}\tau}} \left(1 - e^{-\frac{(t-t^-)}{\tau_{\text{FAC}}}}\right) + I_{\text{gain}}^{\text{TRG}-} e^{-\frac{(t-t^-)}{\tau_{\text{FAC}}}} & \text{(discharge phase)} \\ I_{\text{gain}}^{\text{TRG}-} + (I_{\text{gain}}^{\text{TRG}+} - I_{\text{gain}}^{\text{TRG}-}) e^{-\frac{(t-t^+)}{\tau_{\text{FAC}}}} & \text{(charge phase)} \end{cases} \quad (14)$$

$$\tau_{\text{TRG}} \frac{dI^{\text{TDE}}}{dt} = I^{\text{TDE}} \left(1 - \frac{1}{I_{\text{TRG}\tau}} \frac{I_w^{\text{TRG}}}{1 + \frac{I^{\text{TDE}}}{I_{\text{gain}}^{\text{TRG}}(t)}}\right) \quad (15)$$

$$\tau_{\text{TRG}} \frac{dI^{\text{TDE}}}{dt} - I^{\text{TDE}} = -\frac{I_w^{\text{TRG}}}{I_{\text{TRG}\tau}} I_{\text{gain}}^{\text{TRG}}(t) \quad (16)$$

$$\tau_{\text{TRG}} \frac{dI^{\text{TDE}}}{dt} + I^{\text{TDE}} = \begin{cases} \frac{I_w^{\text{TRG}}}{I_{\text{TRG}\tau}} I_{\text{gain}}^{\text{TRG}-} & \text{for } t < t^- \\ \frac{I_w^{\text{TRG}}}{I_{\text{TRG}\tau}} \left[\frac{I_w^{\text{FAC}} I_{\text{gain}}^{\text{FAC}}}{I_{\text{FAC}\tau}} \left(1 - e^{-\frac{(t-t^-)}{\tau_{\text{FAC}}}}\right) + I_{\text{gain}}^{\text{TRG}-} e^{-\frac{(t-t^-)}{\tau_{\text{FAC}}}} \right] & \text{for } t^- \leq t < t^+ \\ \frac{I_w^{\text{TRG}}}{I_{\text{TRG}\tau}} \left[I_{\text{gain}}^{\text{TRG}-} + (I_{\text{gain}}^{\text{TRG}+} - I_{\text{gain}}^{\text{TRG}-}) e^{-\frac{(t-t^+)}{\tau_{\text{FAC}}}} \right] & \text{for } t \geq t^+ \end{cases} \quad (17)$$

We analyse the case for $t \geq t^+$, translating to a trigger pulse arriving after the end of a facilitator pulse.

$$\tau_{\text{TRG}} \frac{dI^{\text{TDE}}}{dt} + I^{\text{TDE}} = \frac{I_w^{\text{TRG}}}{I_{\text{TRG}\tau}} \left[I_{\text{gain}}^{\text{TRG}-} + (I_{\text{gain}}^{\text{TRG}+} - I_{\text{gain}}^{\text{TRG}-}) e^{-\frac{t}{\tau_{\text{FAC}}}} \right] \quad (18)$$

$$I^{\text{TDE}}(t) = \begin{cases} \left[1 - e^{-\frac{t-t_{\text{TDE}}^-}{\tau_{\text{TRG}}}} \right] \frac{I_w^{\text{TRG}} I_{\text{gain}}^{\text{TRG}-}}{I_{\text{TRG}\tau}} + I^{\text{TDE}-} e^{-\frac{t-t_{\text{TDE}}^-}{\tau_{\text{TRG}}}} \\ + \frac{\tau_{\text{FAC}}}{\tau_{\text{FAC}} - \tau_{\text{TRG}}} \frac{I_w^{\text{TRG}}}{I_{\text{TRG}\tau}} (I_{\text{gain}}^{\text{TRG}+} - I_{\text{gain}}^{\text{TRG}-}) \left[e^{-\frac{t_{\text{TDE}}^- - t}{\tau_{\text{FAC}}}} - e^{-\frac{t-t_{\text{TDE}}^-}{\tau_{\text{TRG}}}} \right] e^{-\frac{t-t_{\text{TDE}}^-}{\tau_{\text{FAC}}}} & \text{(discharge phase)} \\ I^{\text{TDE}+} e^{-\frac{(t-t_{\text{TDE}}^+)}{\tau_{\text{TRG}}}} & \text{(charge phase)} \end{cases} \quad (19)$$

Consider discharge phase at $t = t_{\text{TDE}}^- + \delta t = t_{\text{TDE}}^+$ where $\delta t \ll t_{\text{TDE}}^-$

$$I^{\text{TDE}}(t_{\text{TDE}}^- + \delta t) \approx -\frac{\delta t}{\tau_{\text{TRG}}} \frac{I_w^{\text{TRG}} I_{\text{gain}}^{\text{TRG}-}}{I_{\text{TRG}\tau}} + I^{\text{TDE}-} \left(1 - \frac{\delta t}{\tau_{\text{TRG}}}\right) + \frac{\tau_{\text{FAC}}}{\tau_{\text{FAC}} - \tau_{\text{TRG}}} \frac{I_w^{\text{TRG}}}{I_{\text{TRG}\tau}} (I_{\text{gain}}^{\text{TRG}-} - I_{\text{gain}}^{\text{TRG}+}) \left[\frac{\delta t}{\tau_{\text{FAC}}} - \frac{\delta t}{\tau_{\text{TRG}}} \right] e^{-\frac{t_{\text{TDE}}^-}{\tau_{\text{FAC}}}} \quad (20)$$

If we assume $I^{\text{TDE}-} \approx 0$ the result is a dependence on the time of arrival of the facilitator pulse t_{TDE}^- on the maximum current drawn from M_{10} .

$$I^{\text{TDE}+} \propto e^{-\frac{t_{\text{TDE}}^-}{\tau_{\text{FAC}}}} \quad (21)$$

S2. ARRE

The ARRE is defined as follows: P is a vector of the predicted Euler angles and G the ground truth, at each measurement time step. $\log_m(\cdot)$ is matrix logarithm and $\|\cdot\|_2$ is the $L2$ norm.

$$\text{ARRE}(P, G) = \frac{1}{n} \sum_{i=1}^n \|\log_m(P_i^T G_i)\|_2 \quad (22)$$

S3. SILICON NEURON

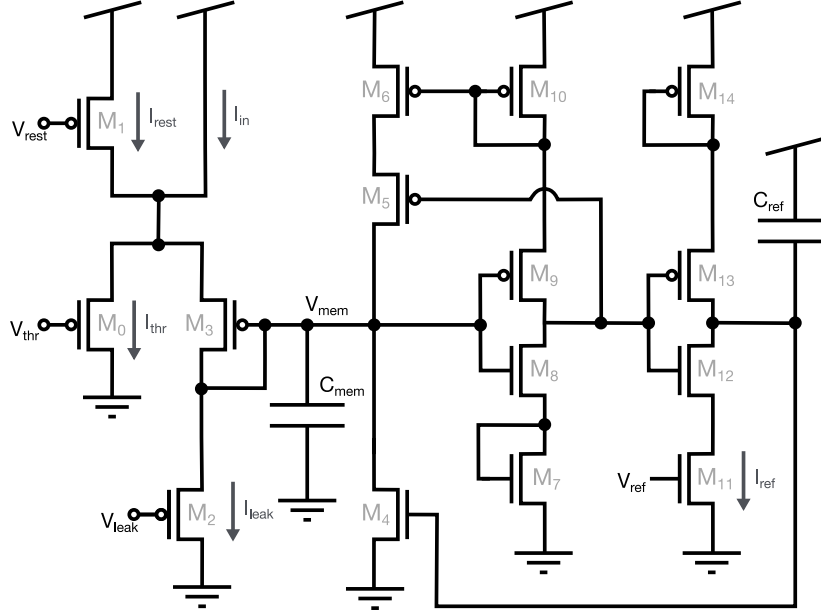


*Fig. S1: The silicon neuron circuit used in the TDE implementation on the *cognigr1* ASIC [2–4]. Within the neuron, the input current results from the combination of I_{in} and I_{rest} . I_{rest} is a current employed to establish the resting voltage level across C_{mem} , representing the membrane potential V_{mem} . The inverter, $M_8 - M_9$, switches when the membrane voltage reaches a its switching threshold. Upon switching, the current passing through it, I_{mem} , increases. This consequently triggers a positive feedback loop through the current mirror $M_6 - M_{10}$, causing the amplification current I_{mem} , to further increase V_{mem} . As the output of the initial inverter transitions to a low state, the second inverter, $M_{13} - M_{12}$, initiates the charging of capacitor C_{ref} . The voltage on C_{ref} triggers M_4 to become conductive, leading to the discharge of C_{mem} with a current I_{ref} , ultimately resetting the neuron. However, due to the time required for the capacitor to charge, this negative feedback mechanism operates more slowly than the positive feedback, resulting in the generation of a spike. Following the discharge of V_{mem} until the output of the first inverter returns to a high state, C_{ref} undergoes a gradual discharge through M_4 , with a current determined by V_{ref} . This establishes a designated refractory period, during which C_{mem} experiences continuous discharge through M_4 meaning that the neuron circuit cannot generate a spike.*

S4. PARAMETERS

Circuit bias	Value
I_{τ}^{TRG}	2 pA
I_w^{TRG}	4 nA
I_{τ}^{FAC}	2 pA
I_w^{FAC}	4 nA
I_{gain}^{FAC}	10 pA
I_{ref}	2 pA
I_{leak}	2 pA
I_{rest}	2 pA
I_{thr}	2 pA

(a) TDE circuit

Simulation parameter	Value
u_{θ}	50
τ_{FAC}	20 ms
τ_{TRG}	20 ms
τ_m	20 ms
w^{FAC}	1
w^{TRG}	1
τ_A	0.75 s
t_{ref}	0.1 ms

(b) Brian2

Simulation parameter	Value
u_{θ}	50
τ_{FAC}	20 ms
τ_{TRG}	20 ms
τ_m	20 ms
w^{FAC}	1
w^{TRG}	1
τ_A	10 ms

(c) JAX

*Fig. S2: a) Circuit biases used for all on-chip TDE measurements and experiments. b) Parameters used in *Brian2* simulations. c) Parameters used in *JAX* simulations.*

SUPPLEMENTARY REFERENCES

- [1] C. Bartolozzi and G. Indiveri, “Synaptic Dynamics in Analog VLSI”, *Neural Computation*, vol. 19, no. 10, pp. 2581–2603, 2007. DOI: 10.1162/neco.2007.19.10.2581.

- [2] O. Richter, H. Grotorex, B. Hucko, M. Cotteret, W. Soares Girao, E. Janotte, M. Mastella, and E. Chicca, “A Subthreshold Second-Order Integration Circuit for Versatile Synaptic Alpha Kernel and Trace Generation,” in *Proceedings of the 2023 International Conference on Neuromorphic Systems*, ser. ICONS '23, New York, NY, USA, 2023. DOI: 10.1145/3589737.3606008.
- [3] M. Cotteret, O. Richter, M. Mastella, H. Grotorex, E. Janotte, W. S. Girão, M. Ziegler, and E. Chicca, “Robust Spiking Attractor Networks with a Hard Winner-Take-All Neuron Circuit,” in *2023 IEEE International Symposium on Circuits and Systems (ISCAS)*, 2023, pp. 1–5. DOI: 10.1109/ISCAS46773.2023.10181513.
- [4] M. Mastella, H. Grotorex, M. Cotteret, E. Janotte, W. Soares Girao, O. Richter, and E. Chicca, “Synaptic Normalisation for On-Chip Learning in Analog CMOS Spiking Neural Networks,” in *Proceedings of the 2023 International Conference on Neuromorphic Systems*, ser. ICONS '23, New York, NY, USA, 2023. DOI: 10.1145/3589737.3606007.